Int. J. Electrochem. Sci., 11 **(2016)** 9644 – 9655, doi: 10.20964/2016.11.48

International Journal of ELECTROCHEMICAL SCIENCE
www.electrochemsci.org

Facile Preparation of MnO_2 with Large Surface Area in a Rotor–Stator Reactor for Supercapacitors

Ya Ling Li[1,2,3], *Lu Hai Li*[3], *Guang Wen Chu*[1,2], *Xiao Fei Zeng*[1,2], *Jian Feng Chen*[1,2], *Lei Shao*[1,2,*]

[1] State Key Laboratory of Organic–Inorganic Composites, Beijing University of Chemical Technology, Beijing 100029, PR China
[2] Research Center of the Ministry of Education for High Gravity Engineering and Technology, Beijing University of Chemical Technology, Beijing 100029, PR China
[3] Beijing Engineering Research Center of Printed Electronics, Beijing Institute of Graphic Communication, Beijing 102600, PR China
[*]E-mail: shaol@mail.buct.edu.cn

Received: 14 August 2016 / *Accepted:* 17 September 2016 / *Published:* 10 October 2016

Facile preparation of MnO_2 with large specific surface area was explored in a rotor–stator reactor (RSR). The MnO_2 product was characterized by FESEM, TEM, XRD, XPS, TG, FTIR and automated surface area and pore size analyzer. The electrochemical performance of the as-prepared MnO_2 nanospheres as an electrode material for supercapacitors was investigated using three-electrode and two-electrode methods. The results show that the MnO_2 nanospheres were well dispersed and had a surface area of 337.01 m^2 g^{-1}. The specific capacitance was as high as 320.7 F g^{-1} at 0.3 A g^{-1} and 477.5 F g^{-1} at 5 mV s^{-1}. The as-prepared MnO_2 also exhibited good stability with 107.4 % capacitance retention after 1000 cycles. Moreover, the MnO_2//active carbon asymmetric supercapacitor in 1 M Na_2SO_4 electrolyte showed a maximum energy density of 27.23 W h kg^{-1} and correspondingly power density was 225 W kg^{-1}.

Keywords: manganese dioxide; rotor–stator reactor; surface area; supercapacitor

1. INTRODUCTION

Supercapacitors have been attracting wide interest due to their high capacitance, long cyclic life and potential application in energy storage devices along with the development of wearable electronics, integrated smart devices and printed electronics [1-6]. In general the performances of supercapacitors depend on the electrode materials and electrolyte. Until now, the major electrode materials can be summarized carbon-based materials (e.g., active carbon, graphene, carbon nanotubes)

[7-10], conductive polymers [11], transition-metal oxides or hydroxides, metal sulfides [12-14], metal-organic frameworks [15] and their composites [16-19]. Among them, transition metal oxides can provide large capacitance because the oxides have several redox states, fast faradic and reversible reactions as well as electric double layer for charge storage.

Manganese dioxide (MnO_2) has been extensively investigated as a promising electrode material due to its high theoretical capacitance (1370 F g^{-1}), natural abundance, diverse crystal forms and environmental friendliness [20]. In order to meet the application needs of flexible energy devices combined with the low-cost and large-scale printing technology, it is necessary to develop MnO_2 particles discussed within this paper. So far, various preparation techniques of MnO_2 particles such as wet chemical method, rheological phase reaction, hydrothermal or solvothermal method, interfacial reaction, microemulsion route, sol-gel method and electrochemical deposition have been studied [21-29]. However, the as-prepared methods exist some disadvantages such as strict operation conditions, low yield and low surface area and thereby as-obtained MnO_2 usually exhibits a relative low specific capacitance [30]. In previous studies, two routes are usually adopted to improve the electrochemical properties of MnO_2. The first one is to make MnO_2-based hybrid or composite materials to boost the conductivity. Another one is to control the crystal structure, particle size or morphology to obtain MnO_2 with porous structure and high specific surface area. The surface area is an important indicator for pure MnO_2 particles. Up to now, the relative large surface area of as-obtained MnO_2 prepared with chemical reduction method achieves only 165.8 m^2 g^{-1} [31].

A novel rotor-stator reactor (RSR) whose structure and specifications were presented in our previous papers [32-34], was employed to prepare MnO_2 in this study based on the following considerations. The RSR technology is suitable for the fast reaction system and continuous production. Moreover, small liquid droplets, thin liquid films and violent turbulence of the reactants resulting from the strong centrifugal force generated by the rotating rotor in the RSR, lead to a significant intensification of micromixing and mass transfer. Micromixing time in the RSR is about 10^{-5} s, which means that a uniform concentration distribution in the RSR can be easily achieved and thus lead to the production of small and uniform particles with large surface area. Finally, the products can be separated immediately with reactants in the RSR, which control the separation of the nucleation and growth processes to avoid the growth of particles.

Herein, we present a facile method to prepare MnO_2 nanospheres with large surface area without any surface active agents using the RSR. The reaction time is relative short and the samples can be easily produced on large scale. The as-prepared MnO_2 products show good electrochemical performances in the application for supercapacitors.

2. EXPERIMENTAL

2.1 Chemicals

Potassium permanganate ($KMnO_4$, AR, >99.5%) was purchased from Sinopharm Chemical Reagent Co., Ltd. Manganese nitrate solution ($Mn(NO_3)_2$, AR, 50 wt.% in water), N-methylpyrrolidone (NMP, 99%) and sodium sulfate (Na_2SO_4, AR, 99 %) were purchased from

Aladdin Reagent Co., Ltd. Active carbon, acetylene black, polyvinylidenefluoride (PVDF, HSV900, Arkema), graphite paper and the separator (NKK TF4030) were purchased from local commercial agents.

2.2 Preparation of MnO_2 nanospheres

The reaction equation is described as Eq.1:

$$2\ KMnO_4 + 3\ Mn(NO_3)_2 + 2\ H_2O = 5\ MnO_2 + 4\ HNO_3 + 2\ KNO_3 \qquad (1)$$

The schematic diagram of the experimental set-up is shown in Fig. 1.

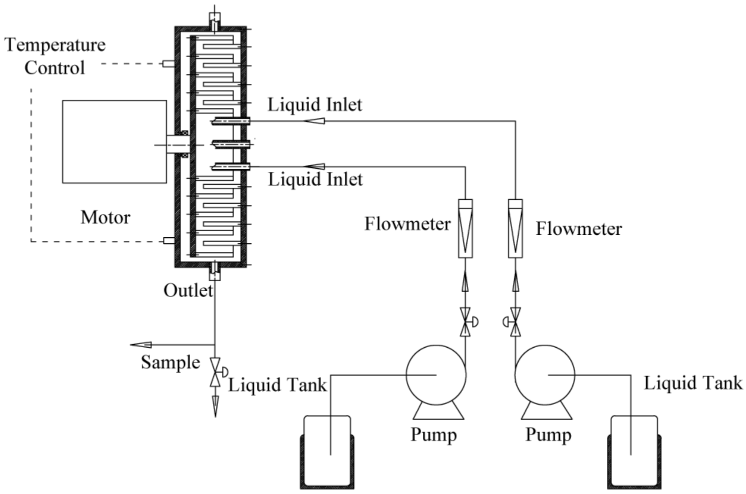

Figure 1. Schematic diagram of the experimental set-up.

Herein only the optimized experimental condition was demonstrated using specific surface area and specific capacitance as evaluation indicators. Firstly, 0.025 M $KMnO_4$ and 0.0375 M $Mn(NO_3)_2$ solutions were heated to 50 ^oC and then pumped simultaneously into the RSR at a flow rate of 12.84 L h^{-1}. $KMnO_4$ and $Mn(NO_3)_2$ mixed and reacted in the RSR with the rotating speed of 900 rpm and the whole reaction process was completed about two minutes. Then, the resulting products was collected from the outlet and filtered and rinsed with distilled water and ethanol. Finally, the product was desiccated at 80 ^oC for 12 h in a vacuum oven to obtain MnO_2 powder.

2.3 Characterization

The as-obtained MnO_2 was characterized on a Hitachi SU8020 field emission scanning electron microscope (FESEM) and a JEOL JEM-1200EX transmission electron microscope (TEM). The crystal structure was measured by a Rigaku Dmax/2200PC X-ray diffractometer (XRD) using Cu Kα radiation (λ=0.15406 nm). The diffraction patterns were recorded from 10 to 80 ^{o} at a scan rate of 5 ^{o} min^{-1}. The chemical valence of Mn was confirmed by a Thermofisher ESCALAB 250Xi X-ray photoelectron spectroscopy (XPS) using Al Kα radiation (1486.71 eV) and correction with C_{1s} line at

284.6 eV. The MnO_2 powders were degasified at 110 °C for using a FLOVAC degasser and then analyzed by N_2 adsorption-desorption at 77 K using a Quantachrome Quadrasorb *SI* surface area and pore size analyzer. The thermal analysis was performed from 30 to 1000 °C at 20 K min^{-1} ramping rate under nitrogen using a Netzsch TG209F3 thermogravimetric (TG) analyzer. The IR spectra of MnO_2 without calcination and calcined at 300 °C were recorded by a Thermo Electron Nicolet 6700 Fourier transform infrared spectrometer (FTIR).

2.4 Electrochemical measurement

The electrochemical measurements including cyclic voltammetry (CV), galvanostatic charge-discharge (GCD) and electrochemical impedance spectroscopy (EIS) were conducted on a Metrohm AUTOLAB PGSTAT302N potentiostat galvanostat. EIS measurement was performed in the frequency range of carried out from 0.1 Hz to 100 k Hz. The stability of the asymmetric supercapacitor was investigated using a LANHE CT2001A battery testing system. The specific capacitance of the MnO_2 electrode (C_{sc} or C_{sp}, F g^{-1}) in three-electrode system was calculated according to Eq. (2) and (3). The specific capacitance of the active electrode (C_s, F g^{-1}) and that of the supercapcatior (C, F g^{-1}), energy density (E, Wh kg^{-1}) and power density (P, W kg^{-1}) in two-electrode method were calculated using the formula from (4) to (6) [35-39]:

$$C_{\mathrm{sc}} = \int idV/(m_1 \times v \times V) \tag{2}$$

$$C_{\mathrm{sp}} = (I \times \Delta t)/(m_1 \times \Delta V) \tag{3}$$

$$C_s = 4C = (2I \times \Delta t)/(m_2 \times \Delta V) \tag{4}$$

$$E = (1/2)C \times \Delta V^2 / 3.6 \tag{5}$$

$$P = E/\Delta t \times 3600 \tag{6}$$

Where $\int idV$ is the integral of CV curves, m_1 is the mass of MnO_2 in single electrode, v is the scan rate of the potential, V is the potential window, I is the applied current, Δt is the discharge time of GCD curves, ΔV is the voltage excluded IR-drop, m_2 is the average mass of MnO_2 and AC in each electrode.

2.4.1 Three-electrode method

The as-prepared MnO_2 powders, acetylene black and PVDF (mass ratio of 80:10:10) were mixed in NMP and then grinded in a mortar for about 30 min to obtain the electrode slurry. The slurry was coated onto a 1 × 2 cm^2 graphite paper within an area of 1 × 1 cm^2, which was subsequently dried at 120 °C for 12 h in an electronic oven to obtain the working electrode. A platinum sheet (1×1 cm^2) and a Ag/AgCl electrode were used as counter and reference electrodes, respectively.

2.4.2 Two-electrode method

Typically, 0.1 g of as-prepared MnO_2, 0.0125 g of acetylene black and 0.0125 g of PVDF were well dispersed in NMP and then a small amount of the as-obtained slurry was dropped onto a circular nickel foam tablets to obtain the MnO_2 electrode which was dried at 110 ^oC for 5 h before compacted at a pressure of 10 MPa. The active carbon (AC) electrode was prepared similarly by using AC instead of MnO_2. Subsequently, the MnO_2 electrode and the AC electrode were assembled into a CR2016 type coin cell with a separator and the electrolyte was 1 M Na_2SO_4 solution.

3. RESULTS AND DISCUSSION

3.1 Morphology and crystal structure

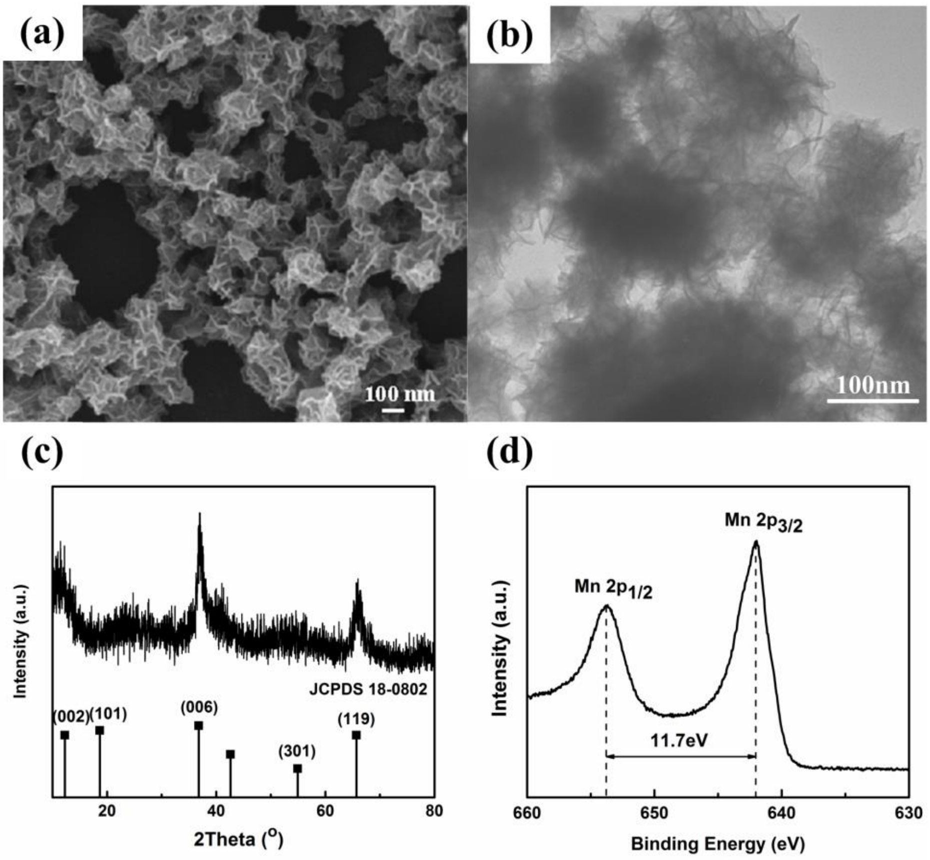

Figure 2. SEM image (a), TEM image (b), XRD pattern (c) and XPS spectrum (d) of MnO_2 prepared in RSR.

The as-prepared MnO_2 has the morphology of petal-shaped nanosheets as shown in Fig.2a and Fig.2b. The MnO_2 nanosheets aggregated into nanospheres. The petals seem very thin and some of them are even transparent from the TEM image in Fig.2b. The as-obtained MnO_2 nanosphere had a diameter of about 200 nm and was smaller than the MnO_2 with a diameter of 400-500 nm reported by Wang et al [40], indicating that smaller MnO_2 crystal nuclei formed in the RSR due to an excellent micromixing effect. Small particles can provide more active sites for charge transfer and reduce diffusion distance of electrolyte ions, thus leading to fast charge/discharge and enhanced capacitive properties.

The XRD pattern of MnO_2 (Fig. 2c) shows that three peaks at 12.3, 36.6 and 65.7 ^{o} correspond to the crystal planes of (002), (006) and (119), respectively (JCPDS No. 18-0802). The crystallographic form of the as-prepared MnO_2 is birnessite-type δ-MnO_2 [40], which has an interlayer distance of about 7Å [20]. And the tunnel size in the crystalline structure is suitable for fast insertion/extraction of hydrated Na^+ cations with a radius of 3.58 Å [41], which is favourable for boosting the capacitance value. The broad peaks at about 12 and 24 ^{o} indicate the crystalline component and amorphous component co-existed in the as-obtained MnO_2 [42]. The previous studies showed that the capacitance performances decrease with increasing crystallinity [43]. The amorphous porous structures favour ion transport because they provide short ion diffusion paths and reversible and fast faradic reactions. Furthermore, these structures allow a full utilization of the active sites of MnO_2 nanosheets in electrochemical reactions.

Fig.2d is the Mn 2p XPS spectrum of the as-prepared MnO_2. Two peaks at 642.0 eV and 653.7 eV are assigned to the Mn $2p_{3/2}$ and Mn $2p_{1/2}$ binding energy, respectively. The spin-energy separation of 11.7 eV between the two peaks is in agreement with the work of Ren et al [44] and Zhao et al [45] and reveals that manganese is in the chemical state of Mn (IV).

3.2 FTIR and TG analysis

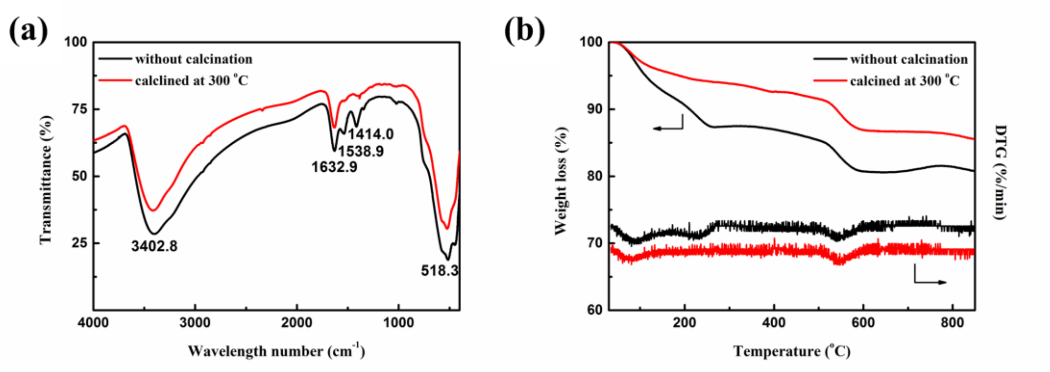

Figure 3. FTIR spectra (a) and TG curves (b) of as-prepared MnO_2 without calcination and calcined at 300 ^{o}C.

The FTIR spectra of MnO_2 without calcination and calcined at 300 ^{o}C for three hours in an atmosphere Muffle furnace are shown in Fig.3a. The absorption at 3402.8 cm^{-1} is attributed to the stretching vibration of –OH group of water molecules [46]. The bands at 1632.9, 1538.9, and 1414.0 cm^{-1} are assigned to the bending vibration of lattice –OH group. The absorption band at 518.3 cm^{-1} is due to the Mn-O vibrations in [MnO_6] octahedra. The intensity of the absorption bands at 1538.9 and 1414.0 cm^{-1} became weak after MnO_2 was calcinated at 300 ^{o}C, demonstrating that MnO_2 prepared in the RSR contains crystal water molecules [46].

TG analysis was used to examine the content of crystal water in the as-prepared MnO_2 and the TG curves are shown in Fig.3b. The weight loss below 105 ^oC was caused by the absorbed water and the weight loss from 105 to 300 ^oC was caused by the crystal water. The second weight loss stage disappeared after the sample was calcinated at 300 ^oC for 3 h, indicating that the crystal water in the as-prepared MnO_2 can be completely removed. The calculated content of the crystal water in $MnO_2{\cdot}xH_2O$ is x=0.24. The weight loss at about 550 ^oC was corresponding to the transformation from MnO_2 to Mn_2O_3 [47].

3.3 Surface area and porosity analyses

The N_2 adsorption/desorption isotherms of the as-prepared MnO_2 and the calculated pore size distribution using the N_2 at 77 K on carbon slit/cylinder pores QSDFT adsorption model are presented in Fig.4.

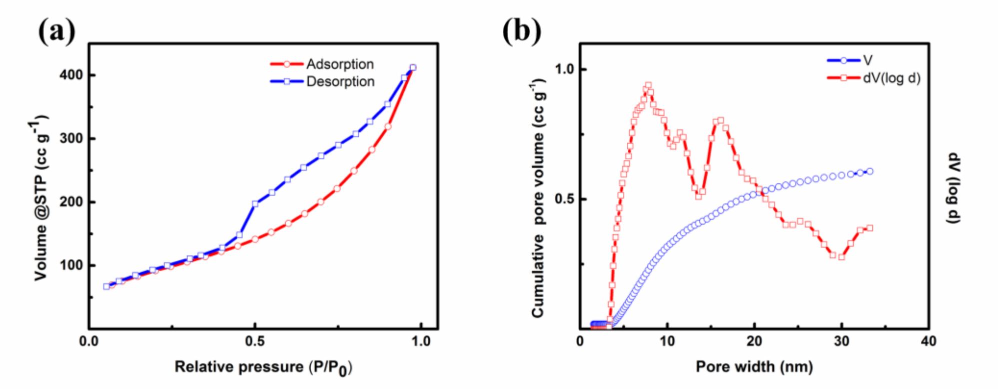

Figure 4. Nitrogen adsorption-desorption isotherm (a) and corresponding pore size distribution (b) of as-prepared MnO_2.

The isotherm curve in Fig.4a exhibits an IUPAC type IV isotherm with a type H3 hysteresis loop, suggesting that the self-assembly of ultrathin MnO_2 nanosheets gave rise to mesoporous structure and slit-shaped pores. The BET surface area was calculated to be 337.01 m^2 g^{-1}, which is much higher than that reported by Dai et al (33.57 m^2 g^{-1}) [48] and Roberts et al (96 to 109 m^2 g^{-1}) [49]. Because the RSR can cause a strong turbulence, there is a high surface renewing rate of the liquid elements and excellent micromixing effect in the RSR, resulting in the production of MnO_2 with a small size and large specific surface area. As shown in Fig.4b, the MnO_2 shows a broad pore size distribution between 3.3 nm and 33 nm, confirming a mesoporous structure. The most probable pore diameter of MnO_2 was 6.376 nm and the total pore volume was 0.608 cc g^{-1}. The large specific surface area and porous structure of MnO_2 provide the possibility of efficient transport of electrons and ions and thus lead to the excellent electrochemical behaviour.

3.4 Electrochemical performance

The mechanisms for the charge storage in MnO_2 electrode are based on the insertion-extraction of M^+ from the electrolyte into the porous MnO_2 matrix (Eq.7) or the adsorption of M^+ on the MnO_2 electrode (Eq. 8) [50].

$$MnO_2 + M^+ + e^- = MMnO_2 \qquad (7)$$

$$(MnO_2)_{surface} + M^+ + e^- = (MnO_2^- M^+)_{surface} \qquad (8)$$

M^+ could be H^+, Li^+, Na^+ and K^+. Among H^+ and the alkali metal cations, Na^+ ions possess a high diffusion rate, adsorption-desorption rate and mobility in aqueous solution and offer MnO_2 the best electrochemical properties [28]. Therefore, the electrochemical studies of the as-prepared MnO_2 were conducted in 1 M Na_2SO_4 electrolyte.

Fig.5a demonstrates the CV curves of the MnO_2 electrode at different scan rates. At a low scan rate of 5 mV s^{-1}, the as-prepared MnO_2 electrode achieved a specific capacitance (C_{sc}) of 477.5 F g^{-1}, which is much larger than the reported values of pure MnO_2 electrodes in Na_2SO_4 electrolyte (118 F g^{-1} at 2 mV s^{-1} [35], 160 F g^{-1} at 5 mV s^{-1} [27, 50] and 347 F g^{-1} at 5 mV s^{-1} [51].

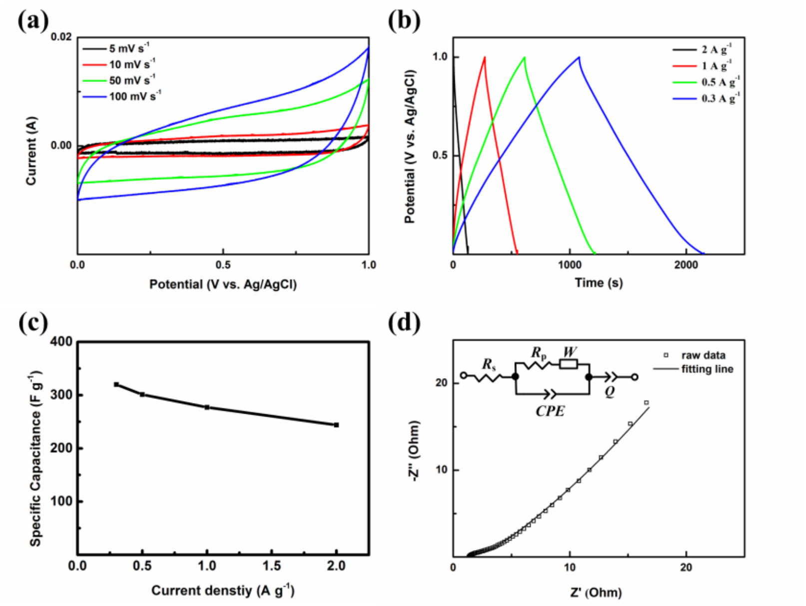

Figure 5. CV curves at various scan rates (a), GCD curves at different current densities (b), specific capacitance versus current densities (c) and Nyquist plot of the MnO_2 electrode (Inset shows the equivalent circuit model) (d).

GCD curves at various current densities of 2, 1, 0.5 and 0.3 A g^{-1} were recorded between 0 and 1.0 V as shown in Fig.5b. The symmetry of the GCD curves and the calculated specific capacitance (Fig.5c) indicate that the as-prepared MnO_2 electrode had excellent capacitance performance. When the discharge current density decreased from 2 A g^{-1} to 0.3 A g^{-1}, the specific capacitance (C_{sp}) of the MnO_2 electrode increased from 243 F g^{-1} to 320.7 F g^{-1} demonstrating the remained high capacitance rate.

Fig.5d shows the impedance spectroscopy of the as-prepared MnO_2 electrode within the frequency range from 0.1 Hz to 10^5 Hz. What's more, the equivalent circuit embedded in the upper inset of Fig.5d was used to fit the EIS data. R_s denotes the combined resistance including the ionic resistance of electrolyte, intrinsic resistance of substrate and contact resistance between the active material and the current collector, and R_{ct} reflects the interfacial charge-transfer resistance.[52] In addition, W is on behalf of the ion diffusion controlled Warburg impedance [48], both $CPE1$ and $CPE2$ are constant phase elements. The calculated R_s and R_{ct} were 1.15 and 2.01 Ω, respectively. The nanosheets with small particle size and large specific surface area enhanced the diffusivity of the electrolyte in the electrode and lowered the charge-transfer resistance. The chi-square method was conducted with NOVA software using kronig-kramers method and χ^2 (Z) equalled to 1.277×10^{-7}, suggesting the fitting results had good reliability.

The cycling stability of the MnO_2 electrode was investigated and the specific capacitance vs. the cycle number at a constant current density of 3 A g^{-1} is shown in Fig.6. Capacitance retention increased to 107.4 % of the initial capacitance in 1000 cycles. The excellent stability might be attributed to the surface chemical activation of the electrode as a result of the increase of the contact area between the electrode and the electrolyte during cycling. Moreover, the EIS spectra of the electrode before and after cycling were shown inset of the Fig.6. The steep slope of the line at low frequencies of the MnO_2 electrode after cycling illustrated a high diffusion rate of electrolyte ions, thus resulting large capacitance.

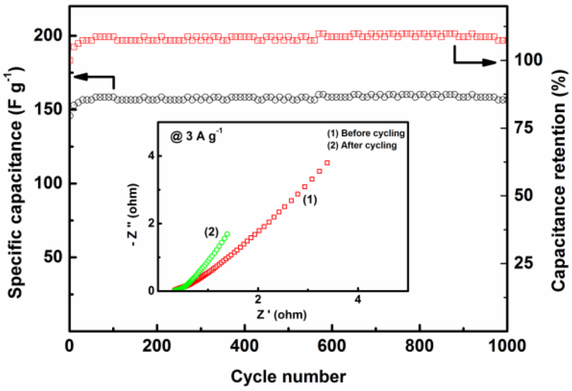

Figure 6. Cycle performance of the MnO_2 electrode measured at a current density of 3 A g^{-1} (Inset shows the EIS spectra of the electrode before and after 1000 cycles).

The MnO_2//AC asymmetric supercapacitor (ASC) was fabricated with a positive electrode (*i.e.* MnO_2 electrode) and a negative electrode (*i.e.* AC electrode) in a 1.0 M Na_2SO_4 electrolyte. Herein, the tested specific capacitance of the AC electrode in three-electrode configuration at a current density of 1 A g^{-1} was 176 F g^{-1}, respectively. The optimum mass ratio of MnO_2 to AC is determined by the formula: $m_+ / m_- = (C_- \times \Delta V_-) / (C_+ \times \Delta V_+)$ in order to balance the charges stored at the two electrodes and obtained an advanced supercapacitor [38, 53]. In this study, the actual mass ratio of the MnO_2 to AC was m (MnO_2) / m (AC) = 0.73 (m (MnO_2) = 3.79 mg and m (AC) = 5.17 mg).

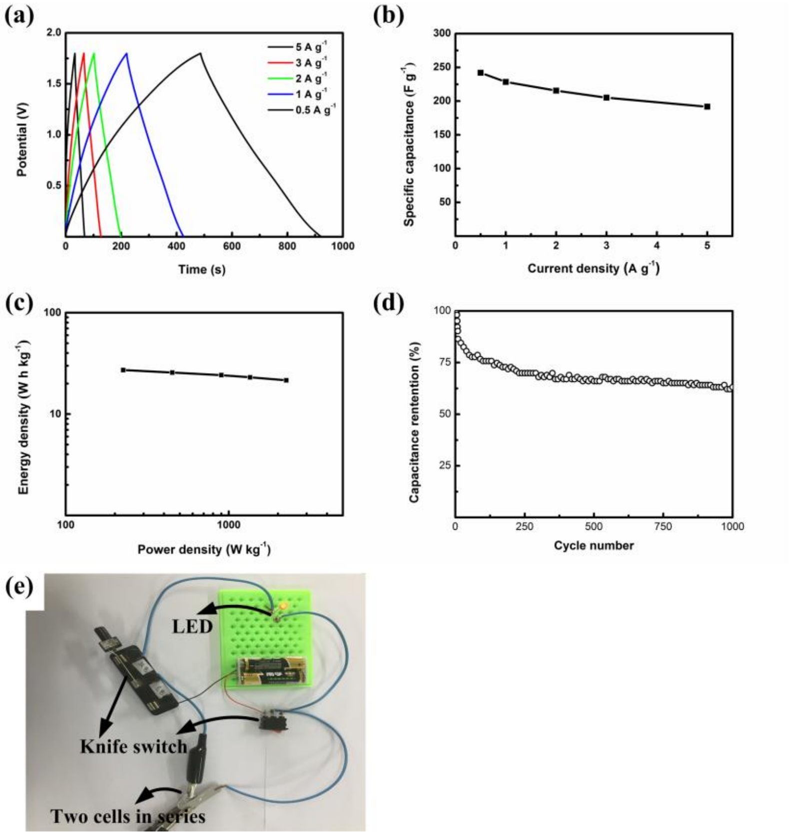

Figure 7. GCD curves at different current densities (a), specific capacitance versus current density (b), Ragone plot related to energy and power densities (c), cycle stability of the MnO_2//AC ASC (d) and photographs showing two asymmetric supercapacitors in series which can light up LED (e).

Fig.7a demonstrates the GCD curves of the MnO_2//AC ASC at different current densities range from 0.5 to 5 A g^{-1} with the potential between 0 and 1.8 V and the specific capacitance (C_s) of the electrode reached a high level of 241.9 F g^{-1} at a current density of 0.5 A g^{-1} (Fig.7b). Fig.7c shows the Ragone plot, *i.e*. a relation curve of energy density (*E*) and power density (*P*). The maximum energy density of the MnO_2//AC was 27.23 W h kg^{-1} at a power density of 225 W kg^{-1}, which is even higher than that of the ASC based on the graphene (GR) and GR-MnO_2 electrodes (GR//GR-MnO_2 23.9 W h kg^{-1}) [54] and the energy density decreased to 21.58 W h kg^{-1} when the power density increased to 2250 W kg^{-1}. Moreover, long-term cycle stability of the MnO_2//AC ASC was also studied through the charge/discharge test at a current density of 1 A g^{-1} (Fig.7d) and the capacitance retention rate was 63.1 % in 1000 cycles. The capacitance fading may be caused by the collapse and dissolving of the active material during the charge-discharge process. It is interesting to observe that two asymmetric supercapacitors in series were able to power a red light-emitting diode (LED) (Fig.7e). These impressive results confirm the excellent performance of MnO_2 prepared in RSR.

4. CONCLUSIONS

In summary, we have developed a facile method to prepare MnO_2 with large surface area in the RSR. The method can be easily scaled up according to the necessary and the reaction time was greatly reduced. Such MnO_2 with a large specific surface area of 337.01 m^2 g^{-1} exhibited excellent electrochemical behaviour, such as a high specific capacitance of 320.7 F g^{-1} at 0.3 A g^{-1} and 107.4 % capacitance retention in 1000 cycles based on three-electrode system. The maximum energy density of the fabricated MnO_2//AC ASC was 27.23 W h kg^{-1} at a power density of 225 W kg^{-1}. This RSR technology provides a new pathway for the preparation of metal oxides with large surface area for high energy density supercapacitors.

ACKNOWLEDGEMENTS

This work was supported by the National Natural Science Foundation of China (21403014), Beijing municipal commission of education 2011 collaborative innovation center, printed electronics technology & engineering discipline construction (III)**,** Beijing Municipal Science and Technology Project (Z151100003315005), Beijing Municipal Commission Education (SQKM201710015009) and General Project of BIGC (Eb201602).

References

1 Y. Zheng, Y. Yang, S. Chen, Q. Yuan, *CrystEngComm*, (2016) DOI: 10.1039/C5CE02510A.
2 J. Yun, Y. Lim, G. N. Jang, D. Kim, S.J. Lee, H. Park, S. Y. Hong, G. Lee, G. Zi, J. S. Ha, *Nano Energy*, 19 **(**2016) 401.
3 I. Ryu, G. Kim, D. Park, S. Yim, *J. Power Sources*, 297 (2015) 98.
4 Y. Tian, S. Cong, W. Su, H. Chen, Q. Li, F. Geng, Z. Zhao, *Nano letters*, 14 (2014) 2150.
5 S. Cho, M. Kim, J. Jang, *ACS Appl. Mater. interfaces*, 7 (2015) 10213.
6 *PRC Pat.*, ZL 201410186329.1 (2015).
7 L. L. Zhang, X. S. Zhao, *Chem. Soc. Rev.*, 38 (2009) 2520.
8 X. Peng, L. Peng, C. Wu, Y. Xie, *Chem. Soc. Rev.*, 43 (2014) 3303.
9 Y. B. Tan, J. M. Lee, *J. Mater. Chem. A*, 1 (2013) 14814.
10 Z. Q. Wen, M. Li, S. J. Zhu, T. Wang, *Int. J. Electrochem. Sci*., 11(2016) 23.
11 I. Shown, A. Ganguly, L. C. Chen, K. H. Chen, *Energy Sci. Eng.*, 3 (2015) 2.
12 J. Feng, X. Sun, C. Wu, L. Peng, C. Lin, S. Hu, J. Yang, Y. Xie, *J. Am. Chem. Soc.*, 133 (2011) 17832.
13 K. J. Huang, L. Wang, J. Z. Zhang, L. L. Wang, Y. P. Mo, *Energy*, 67 (2014) 234.
14 M. S. Javed, S. Dai, M. Wang, Y. Xi, Q. Lang, D. Guo, C. Hu, *Nanoscale*, 7 (2015) 13610.
15 L. Wang, Y. Han, X. Feng, J. Zhou, P. Qi, B. Wang, *Corros. Chem. Rev.*, 307 (2016) 361.
16 G. Wang, L. Zhang, J. Zhang, *Chem. Soc. Rev.*, 41 (2012) 797.
17 H. Li, L. Jiang, Q. Cheng, Y. He, V. Pavlinek, P. Saha, C. Li, *Electrochim. Acta*, 164 (2015) 252.
18 Z. Yu, L. Tetard, L. Zhai, J. Thomas, *Energy Environ. Sci*., 8 (2015) 702.
19 D. Guo, L. Lai,A. Cao, H. Liu, S. Dou, J. Ma, *RSC Adv*., 5 (2015) 55856.
20 M. Huang, F. Li, F. Dong, Y. X. Zhang, L. L. Zhang, *J. Mater. Chem. A,* 3 (2015) 21380.
21 X. G. Zhang, C. M. Shen, H. L. Li, *Mater. Res. Bull.*, 36 (2011) 541.
22 L. Yuan, Z. Li, J. Sun, K. Zhang, Y. Zhou, *Mater. Lett.*, 57 (2003) 1945.
23 X. Wang, Y. D. Li, *J. Am. Chem. Soc*., 24 (2002) 2880.
24 D. K. Walanda, G. A. Lawrance, S. W. Donne, *J. Power Sources*, 139 (2005) 325.
25 G. H. Yue, P. X. Yan, D. Yan, D. M. Qu, X. Y. Fan, M. X. Wang, H. T. Shang, *J. Cryst. Growth*, 294 (2006) 385.
26 A. K.Thapa, B. Pandit, R. Thapa, T. Luitel, H. S. Paudel, G. Sumanasekera, M. K. Sunkara, N. Gunawardhana, T. Ishihara, M. Yoshio, *Electrochim. Acta*, 116 (2014) 188.

27 D. Yan, H. Zhang, S. Li, G. Zhu, Z. Wang, H. Xu, A. Yu, *J. Alloys Compd.*, 607 (2014) 245.
28 R. N. Reddy, R. G. Reddy, *J. Power Sources*, 124 (2003) 330.
29 Y. Q. Zhao, D. D. Zhao, P. Y. Tang, Y. M. Wang, C. L. Xu, H. L. Li, *Mater. Lett.*, 76 (2012) 127.
30 S. Kong, K. Cheng, T. Ouyang, K. Ye, Y. Gao, G. Wang, D. Cao, *J. Power Sources*, 293 (2015) 519.
31 Y. Chen, C. Liu, F. Li, H. M. Cheng, *J. Alloys Compd.*, 397 (2005) 282.
32 G. W. Chu, Y. H. Song, H. J. Yang, J. M. Chen, H. Chen, J. F. Chen, *Chem. Eng. J*. 128 (2007) 191.
33 Y. Li, G. Chu, B. Sun, J. Chen, L. Shao, *Chem. Eng. Processing*, 87 (2015) 68.
34 Y. Li, S. Wang, B. Sun, M. Arowo, H. Zou, J. Chen, L. Shao, *Chem. Eng. Sci*., 134 (2015) 521.
35 W. Yao, J. Wang, H. Li, Y. Lu, *J. Power Sources*, 247 (2014) 824.
36 L. Demarconnay, E. Raymundo-Piñero, F. Béguin, *J. Power Sources*, 196 (2011) 580.
37 Q. Zheng, Z. Cai, Z. Ma, S. Gong, *ACS Appl. Mater. interfaces*, 7 (2015) 3263.
38 H. Niu, D. Zhou, X. Yang, X. Li, Q. Wang, F. Qu, *J. Mater. Chem. A*, 3 (2015) 18413.
39 W. Xu, B. Mu, W. Zhang, A. Wang, *RSC Adv*., 5 (2015) 64065.
40 C. H. Wang, H. C. Hsu, J. H. Hu, *J. Power Sources*, 249 (2014) 1.
41 T. N. Reddy, R. G. Reddy, *J. Power Sources*, 124 (2003) 330.
42 Y. Ren, N. Yan, J. Feng, J. Ma, Q. Wen, N. Li, Q. Dong, *Mater. Chem. Phys*., 136 (2012) 538.
43 J. X. Feng, S. H. Ye, X. F. Lu, Y. X. Tong, G.R. Li, *ACS Appl. Mater. Interfaces*, 7 (2015) 11444.
44 Y. Ren, N. Yan, Q. Wen, Z. Fan,T. Wei, M. Zhang, J. Ma, *Chem. Eng. J*., 175 (2011) 1.
45 L. Zhao, J. Yu, W. Li, S. Wang, C. Dai, J. Wu, X. Bai, C. Zhi, *Nano Energy*, 4 (2014) 39.
46 L. Su, L. Gong, H. Lü, Q. Xü, *J. Power Sources*, 248 (2014) 212.
47 L. I. Hill, A. Verbaere, D. Guyomard, *J. Power Sources*, 119-121 (2003) 226.
48 X. Dai, W. Shi, H. Cai, R. Li, G. Yang, *Solid State Sci*., 27 (2014) 17.
49 A.J. Roberts, R.C.T. Slade, *Electrochim. Acta*, 55 (2010) 7460.
50 V. Subramanian, H. Zhu, B. Wei, *J. Power Sources*, 159 (2006) 361.
51 G. Zhu, L. Deng, J. Wang, L. Kang, Z.H. Liu, *Colloids Surf. A* , 434 (2013) 42.
52 X. Zhang, X. Sun, H. Zhang, C. Li, Y. Ma, *Electrochim. Acta*, 132 (2014) 315.
53 H. Yi, H. Wang, Y. Jing, T. Peng, Y. Wang, J. Guo, Q. He, Z. Guo, X. Wang, *J. Mater. Chem. A*, 3 (2015) 19545.
54 G. Zhang, L. Ren, L. Deng, J. Wang, L. Kang, Z. H. Liu, *Mater. Res. Bull.*, 49 (2014) 577.